AGU PUBLICATIONS

JGR

Journal of Geophysical Research: Oceans

RESEARCH ARTICLE

10.1002/2013JC009412

Key Point:
- New wind-over-wave-coupling model

Correspondence to:
V. Kudryavtsev,
kudr@rshu.ru

Citation:
Kudryavtsev, V., B. Chapron, and V. Makin (2014), Impact of wind waves on the air-sea fluxes: A coupled model, *J. Geophys. Res. Oceans*, *119*, 1217–1236, doi:10.1002/2013JC009412.

Received 6 SEP 2013
Accepted 2 FEB 2014
Accepted article online 7 FEB 2014
Published online 20 FEB 2014

Impact of wind waves on the air-sea fluxes: A coupled model

V. Kudryavtsev[1], B. Chapron[1,2], and V. Makin[3]

[1]Satellite Oceanography Laboratory, Russian State Hydrometeorological University (RSHU), St. Petersburg, Russia, [2]Laboratoire d'Océanographie Spatiale, Ifremer, Plouzane, France, [3]Royal Netherlands Meteorological Institute, De Bilt, Netherlands

Abstract A revised wind-over-wave-coupling model is developed to provide a consistent description of the sea surface drag and heat/moister transfer coefficients, and associated wind velocity and temperature profiles. The spectral distribution of short wind waves in the decimeter to a few millimeters range of wavelengths is introduced based on the wave action balance equation constrained using the Yurovskaya et al. (2013) optical field wave measurements. The model is capable to reproduce fundamental statistical properties of the sea surface, such as the mean square slope and the spectral distribution of breaking crests length. The surface stress accounts for the effect of airflow separation due to wave breaking, which enables a better fit of simulated form drag to observations. The wave breaking controls the overall energy losses for the gravity waves, but also the generation of shorter waves including the parasitic capillaries, thus enhancing the form drag. Breaking wave contribution to the form drag increases rapidly at winds above 15 m/s where it exceeds the nonbreaking wave contribution. The overall impact of wind waves (breaking and nonbreaking) leads to a sheltering of the near-surface layer where the turbulent mixing is suppressed. Accordingly, the air temperature gradient in this sheltered layer increases to maintain the heat flux constant. The resulting deformation of the air temperature profile tends to lower the roughness scale for temperature compared to its value over the smooth surface.

1. Introduction

Wind generated ocean surface waves provide a feedback on the airflow above by extracting energy and momentum from the wind, thus reducing the wind forcing generating these waves. Starting from earlier papers by *Janssen* [1989] and *Chalikov and Makin* [1991], the wave feedbacks on momentum fluxes in the near-surface atmosphere have been extensively investigated [e.g., *Makin et al*., 1995; *Makin and Mastenbroek*, 1996; *Makin and Kudryavtsev*, 1999; *Hara and Belcher*, 2004; *Chalikov and Rainchik*, 2010]. The basic physics of the wave feedback involves the partitioning of momentum flux in the atmospheric wave boundary layer into turbulent and wave-induced components. Momentum input from wind to waves is proportional to the turbulent stress within an inner region (IR) [*Belcher and Hunt*, 1993]. Therefore, momentum uptake by longer waves reduces wind input to shorter waves, thus their spectral level. This feedback between turbulent stresses and wind waves ensures a stability of the coupled wind wave system [*Kudryavtsev et al*., 1999; *Hara and Belcher*, 2002].

Kudryavtsev et al. [1999] have emphasized that wavelength range from capillaries to the spectral peak must be modeled to ensure a quantitative correspondence with fundamental integral properties of the sea surface, such as the mean square slope (MSS) [e.g., *Cox and Munk*, 1954; *Munk*, 2009]. Indeed, the form drag scaled by the friction velocity squared is directly linked to the MSS [*Plant*, 1982]. MSS is very sensitive to the high-frequency spectrum tail. Unrealistic simulation of MSS would result in unrealistic air-sea fluxes and the form drag. We next show that constrained coupling between wind wave spectrum and related drag coefficient largely overcomes an impact of the turbulent closure scheme—either a simple mixing length closure [e.g., *Makin et al*., 1995] or a higher level closure employing turbulent kinetic energy and its dissipation balance [*Makin and Mastenbroek*, 1996; *Hara and Belcher*, 2004; *Chalikov and Rainchik*, 2012].

Even given a constrained wave spectrum and correct MSS, models systematically underestimate the sea surface drag coefficient [see e.g., *Makin and Kudryavtsev*, 1999, Figure 3; *Kudryavtsev and Makin*, 2001, Figure 1]. Implicitly, this underestimation suggests that impacts of other factors, like wave breakings [e.g., *Melville*, 1977] should be taken into account. Impacts of the airflow separation due to wave breaking on the form

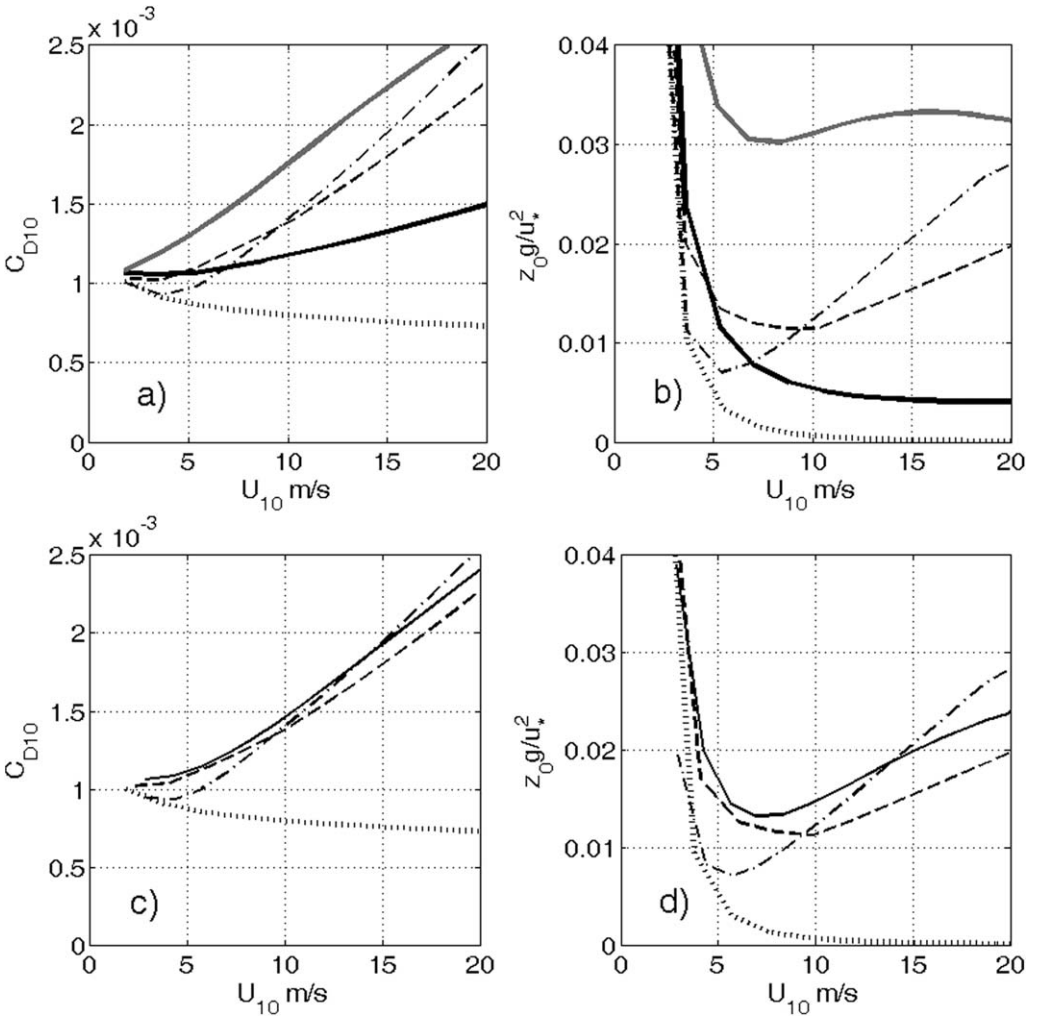

Figure 1. (a and c) Drag coefficient and (b and d) the Charnock parameter versus wind speed. Dash and dash-dotted lines show empirical relations suggested by *Fairall et al*. [2003], COARE 3.0, and *Edson et al*. [2013], COARE 3.5, correspondingly; dotted lines show the smooth surface relations with the roughness scale defined by $z_{0\nu}=0.1\nu/\tau_0^{1/2}$. Solid black and gray lines in Figures 1a and 1b are model calculations without accounting for the AFS, and with "true" MSS (black solid) and with MSS increased twofold (solid gray). Solid lines in Figures 1c and 1d are the full model calculations with accounting for the AFS stress.

drag have been clearly identified by experiments [e.g., *Banner*, 1990; *Reul et al*., 2007] and numerical large eddy simulations (LES) [*Suzuki et al*., 2013].

Effect of the airflow separation from breaking waves on the sea surface drag was first introduced by *Kudryavtsev and Makin* [2001]. They considered the integrated-over-height momentum conservation equation where the form drag is separated between contributions from nonbreaking and breaking waves. The latter is chosen to restitute airflow separations from breaking wave crests that leads to the air pressure drop inside the separation bubbles, thus acting on the forward slope and contributing to the form drag. As shown, the airflow separation can support up to 50% of the total form drag. *Kukulka et al*. [2007] and *Kukulka and Hara* [2008a, 2008b] further developed *Kudryavtsev and Makin*'s [2001] model using vertically resolved momentum conservations equation coupled with wind waves and wave breaking.

In the present study, we follow the approach described above and build upon the recent field observations of 2-D wave number short wind wave spectra (in the wavelength range from a few millimeters to a few decimeters, *Yurovskaya et al*., [2013]) and wave breaking statistics [*Sutherland and Melville*, 2013]. Wave breaking plays an important role in dynamics of "wind wave" coupled system, and their impact is included

in the model through the following mechanisms. Wave breaking (i) controls energy dissipation and thus define spectrum in the gravity range [*Phillips*, 1985]; (ii) generates shorter (including parasitic) surface waves, and thus influence shape of the spectrum in the high-frequency range [e.g., *Kudryavtsev and Johannessen*, 2004; *Rozenberg and Ritter*, 2005]; (iii) enhances the form drag due to the airflow separations from breaking crests and momentum flux to shortwaves generated by breaking crests. At higher wind speeds, outburst of spume droplets from breaking crests [*Veron et al*., 2012] can possibly become important factor affecting dynamics of the coupled system through impact of spray on stratification [*Kudryavtsev*, 2006], and/or direct impact on momentum balance [*Andreas*, 2004; *Kudryavtsev and Makin*, 2011]. Hereafter, we are focusing on dynamics of the coupled system and air-sea fluxes at moderate to high wind speeds, up to about 20 m/s, when impact of sea spray should be negligible.

The main objective of this paper is to develop a model consistently describing the basic components of the wind wave coupled system including the form drag, heat/moister transfer coefficients, vertical wind velocity and temperature profiles, and wave spectrum for meter to millimeter wavelengths. As mentioned, key role in this new development belongs to the wave breaking that control energy losses for the gravity waves and energy gain for shorter surface waves, as well as support significant part of the surface form drag. For all these processes, the same statistical quantity, i.e., the length of breaking wave crests is used.

A consistent coupled wind wave model can also be invoked to analyze and interpret ocean remote sensing measurements. Via the ever-increasing complement of microwave and optical techniques, combined passive and active observations, or polarization properties [e.g., *Hwang et al*., 2010; *Kudryavtsev et al*., 2012, 2013], improved knowledge of the wind wave system, and more particularly the short scale slope and curvature variances, shall help more direct quantifications of air-sea momentum, heat, and gas exchanges.

The paper is organized as the following. In section 2, the momentum conservation equation for narrow band surface waves is considered to introduce the form drag supported by regular (nonbreaking) and breaking waves. We then derive the general momentum conservation equation integrated over all surface waves. In section 3, the wind wave spectrum model and turbulent closure scheme accounting for the impact of breaking waves are introduced followed by discussions of parameterization of some basic surface properties including the length of breaking crests. Then a solution of the coupled problem in terms of the momentum and heat transfer is presented. In section 4, the crucial role of wave breakings on the dynamics of the coupled system is emphasized. Next, we compare model predictions with empirical data. In section 5, we discuss impact of "uncertainties" in definition of the wave spectrum on the drag coefficient, and then discuss an alternative approach for modeling the form drag supported by breaking crests. Conclusions follow in section 6.

2. Momentum Balance

2.1. Narrow Band Wind Waves

Considering an impact of a narrow band (wave number vector range from $\boldsymbol{k}$ to $\boldsymbol{k}+d\boldsymbol{k}$) surface waves and their breakings, the momentum conservation equation (written in the displaced coordinate system following the surface) is decomposed as:

$$\frac{\partial}{\partial z}\overline{u'w'} = -d\tau_w\delta(z-l) - d\tau_s\delta(z-l_b) \tag{1}$$

Here z is the vertical coordinate, $\overline{u'w'}$ is the turbulent momentum flux normalized by the air density (hereinafter all components of the momentum balance are scaled by the air density), $d\tau_w$ is the wave-induced stress, $d\tau_s$ is the stress supported by breaking crests (hereafter called the airflow separation, AFS, stress), and $\delta(z)$ is the Dirac delta-function. As expressed in (1), an expected impact of wind waves is distributed in the vertical. Characteristic vertical scale for breaking crests is $l_b = \varepsilon_b k^{-1}$, where ε_b is the local breaking wave steepness, while the scale for regular (nonbreaking) waves is $l = \varepsilon_l k^{-1}$, where ε_l is the inner region (IR) parameter of an order of $O(10^{-1})$.

Omitting the AFS term, $d\tau_s \equiv 0$, equation (1) corresponds to the momentum balance previously considered by *Kudryavtsev and Makin* [1999], *Kudryavtsev et al*. [1999], and *Hara and Belcher* [2002, 2004]. When both wave-induced and AFS stress components are retained, equation (1) corresponds to the momentum

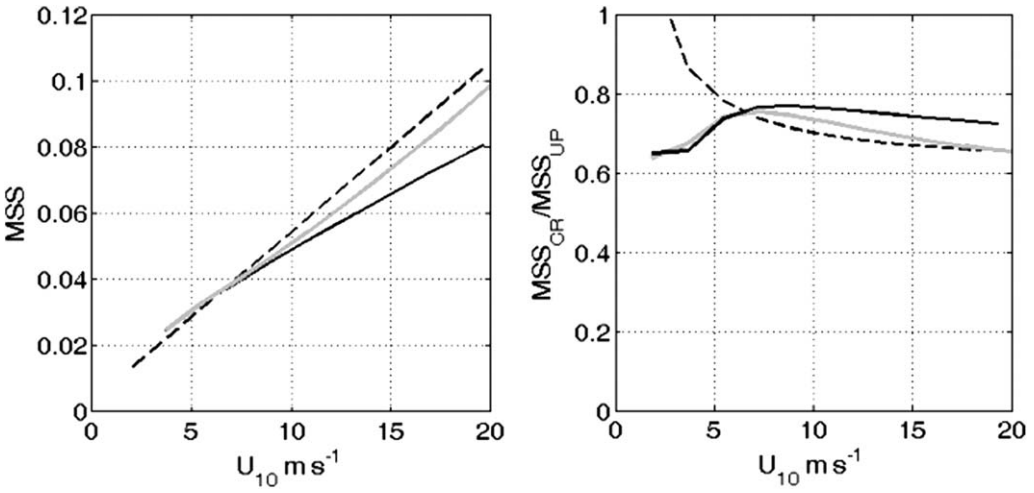

Figure 2. (left) The mean square slope (MSS) of the sea surface and (right) ratio of the cross-wind to the up-wind components of the MSS versus wind speed: dash lines are *Cox and Munk* [1954] data; solid lines are the model calculations; gray solid lines are the model calculations without accounting for the impact of wave breaking stress.

balance considered by *Kudryavtsev and Makin* [2001] using a height-integrated version of (1), and by *Kukulka et al*. [2007], *Kukulka and Hara* [2008a, 2008b]. In fact [see, e.g., *Makin and Kudryavtsev*, 1999, Figure 2; *Sullivan et al*., 2000, Figure 12], the vertical distribution of $d\tau_w$ and $d\tau_s$ can differ from a step-like behavior introduced in (1). However, in the next, we deal with the momentum quantities integrated over all breaking waves (see equations (5) and (8)). Therefore, the details of vertical profiles of $d\tau_w$ and $d\tau_s$ are not important, and only does matter the vertical scales l and l_b of their attenuation.

Wave-induced stress $d\tau_w$ can be directly expressed in terms of wind wave parameters:

$$d\tau_w=(\rho_w/\rho_a)\cos\varphi\beta\omega^2k^{-4}B(\boldsymbol{k})d\boldsymbol{k} \tag{2}$$

where ρ_a and ρ_w are air and water densities, $B(\boldsymbol{k})$ is the saturation spectrum that is related to the wave elevation spectrum, $S(\boldsymbol{k})$, as: $S(\boldsymbol{k})=k^{-4}B(\boldsymbol{k})$, ω and $\boldsymbol{k}$ are wave frequency and wave number vector (k denotes its modulus), β is the wind wave growth rate. The growth rate β is parameterized in the functional form originally suggested by *Plant* [1982] with some modifications suggested by the rapid distortion theory of *Belcher and Hunt* [1993]:

$$\beta=c_\beta\hat{\tau}_l(u_*/c)^2\cos\varphi|\cos\varphi| \tag{3}$$

where c_β is a growth rate "constant" (fixed here at $c_\beta=3\times10^{-2}$), $\hat{\tau}_l=\tau_l(z)/u_*^2$ is the dimensionless turbulent shear stress at the top of the inner region (IR, $z=l\propto0.1k^{-1}$) normalized by the friction velocity, u_*, well above the water surface, c is the phase speed, φ is the direction between wave number vector and wind velocity. Factor $\hat{\tau}_l$ in (3) indicates that growth rate is governed by the turbulent stress in the IR [e.g., *Makin and Kudryavtsev*, 1999, Figure 1]. Notice that we use growth rate (3) for wind waves with phase velocity $c<u_k$, u_k is wind speed at $z=k^{-1}$, while for fast moving waves (with $c>u_k$) $\beta=0$.

Based on similarity between the crest of a breaking wave and a backward step, *Kudryavtsev and Makin* [2001] have proposed the following expression for the airflow separation (AFS) stress, $d\tau_s$:

$$\begin{aligned} d\tau_s&=2\varepsilon_b\Delta p\cos\varphi k^{-1}\Lambda d\boldsymbol{k}\\ \Delta p&=c_{db}(u_b\cos\varphi-c)^2 \end{aligned} \tag{4}$$

where ε_b is the steepness of breaking wave, $\Lambda(\boldsymbol{k})$ the spectral density of length of wave breaking fronts per unit area [*Phillips*, 1985], Δp is the pressure drop (normalized by the air density) due to AFS acting on the forward slope of breaking wave, u_b is the mean wind velocity at the height of breaking crest, and

$z=\varepsilon_b/k$, c_{db} is dimensionless the AFS constant corresponding to the local drag coefficient of breaking crest. Note that while being practical, this analogy is certainly a strong idealization and could not describe well the real breaking process. In principle, a wave can start breaking along one-dimensional crest. But, as it is commonly observed, breaking is often accompanied by intense crest disruptions that produce egg-like roughness patterns with entrainment of the air and results in appearance of well visible whitecaps. In section 5, we shall discuss how to treat (4) in such a complex case.

2.2. Contribution of All Waves

The total AFS force, $T_s(z)$, is given by integration over $\boldsymbol{k}$:

$$T_s(z)=\int\int d\tau_s\delta(z-\varepsilon_b/k)kdkd\varphi \tag{5}$$

Using $d\tau_s$ from (4) and $x=z-\varepsilon_b/k$, (5) becomes:

$$\begin{aligned} T_s(z)&=2\varepsilon_b^2\int\int\Delta p\Lambda\cos\varphi(z-x)^{-2}\delta(x)dxd\varphi\\ &=2\varepsilon_b^2z^{-2}\int(\Delta p\Lambda)_{k=\varepsilon_b/z}\cos\varphi d\varphi \end{aligned} \tag{6}$$

Substituting Δp from (4) gives:

$$\begin{aligned} zT_s(z) &=\left[\hat{T}_s(k)\right]_{k=\varepsilon_b/z}\\ \hat{T}_s(k) &=2\varepsilon_bc_{db}(u_b-c)^2k\Lambda_0\int\lambda_\varphi\cos^3\varphi d\varphi \end{aligned} \tag{7}$$

where $\hat{T}(k)$ is the spectral distribution of the AFS stress, $\Lambda_0(k)=\int\Lambda(k,\varphi)d\varphi$ is the omnidirectional distribution of breaking crests length, and $\lambda_\varphi=\Lambda/\Lambda_0$ is its angular distribution. Notice, that cos φ is factorized from the parentheses in (4) assuming that AFS drag is mostly supported by relatively slow breaking waves.

The wave-induced force T_w integrated over all wave components reads:

$$T_w(z)=\int d\tau_w\delta(z-\varepsilon_l/k)kdkd\varphi \tag{8}$$

Combining (8) and (2) gives:

$$\begin{aligned} zT_w(z)&=\left[\hat{T}_w(k)\right]_{k=\varepsilon_l/z}\\ \hat{T}_w(k)&=c_w\tau_lB_0(k) \end{aligned} \tag{9}$$

where $\hat{T}_w(k)$ is the spectrum of the wave-induced stress, $B_0(k)=\int B(k,\varphi)d\varphi$ is the omnidirectional saturation spectrum, $c_w=(\rho_w/\rho_a)c_\beta\int b_\varphi\cos^3\varphi d\varphi$ is the wave-induced stress "constant," $b_\varphi=B/B_0$ is the angular distribution of wave spectrum.

The momentum conservation equation (1) integrated over all wave components becomes:

$$\frac{\partial\tau}{\partial z}=T_w(z)+T_s(z) \tag{10}$$

where $\tau=-\overline{u'w'}$ is the turbulent stress (scaled by air density). This equation can be rewritten in a "standard" form:

$$\tau(z)+\tau_s(z)+\tau_w(z)=u_*^2 \tag{11}$$

where τ_s and τ_w are the AFS and wave-induced stresses:

$$\tau_s(z)=\int_z^\infty T_s dz, \qquad \tau_w(z)=\int_z^\infty T_w dz \tag{12}$$

expressed via their spectral densities as:

$$\tau_s(z)=\int_0^{\varepsilon_b/z} \hat{T}_s(k) d\ln k, \qquad \tau_w(z)=\int_0^{\varepsilon_l/z} \hat{T}_w(k) d\ln k \tag{13}$$

At the sea surface (11) reads:

$$\tau_{v0}+\int_0^\infty \hat{T}_w(k) d\ln k+\int_0^\infty \hat{T}_s(k) d\ln k=u_*^2 \tag{14}$$

where $\tau_{v0}=\tau(0)$ is the viscous surface stress.

3. The Coupled System

3.1. Spectrum of Wind Waves and Wave Breaking

Spectrum of wind waves determining the form drag of the sea surface is defined following a semiempirical model suggested in *Kudryavtsev et al.* [1999] and *Kudryavtsev and Johannessen* [2004]. It is constrained by the observations [*Yurovskaya et al.*, 2013]. A brief overview of the spectrum is given in Appendix A. The shape of the spectrum in the equilibrium range, from shortest capillaries to wavelengths about 10th of the spectral peak, results from the energy balance, which includes wind forcing (first term in (A1)), viscous and nonlinear (waver breaking) dissipation (first and second term in (A1)), generation of bound parasitic capillary waves, and shortwaves generated by breaking crests due to mechanical disturbances of the sea surface (third term in (A1)). This model is consistent with the measurements (see Figures 6 and 7), and thus can be considered as a "reliable" component of the wind wave coupled model. Coupling of the "water-side" of the model with its "air-side" is done via wind forcing described in terms of the growth rate. In order to have a consistent description of both components of the coupled model, growth rate in the wave spectrum model is defined by the same relation (3) that was used to calculate wave-induced stress (9).

Notice that the energy balance (A1) does not possess a term describing wind energy transfer to breaking crests as suggested by *Kukulka and Hara* [2008a, 2008b]. Although the wind energy flux to breaking crests can be comparable with the flux to "regular" surface (see Figure 4), this term (unlike work of wave-slope-correlated pressure) does not pump energy to the regular surface described by (A1), but provides transient transfer of energy (and momentum) to short-living breaking crests which then transfer the received amount of wind energy and momentum to the turbulence in the upper ocean layer (as well as to spume droplets at high winds). Therefore, wind energy and momentum fluxes to breaking crests should be included in the TKE balance equation for the water side, as this is already done for the air-side (see section 3.2). Usually, the energy flux F_w^{wb}, linked to the wave breaking dissipation (D) as $F_w^{wb}=\int D d\mathbf{k}$, is considered as the main source of TKE in the uppermost meters of the ocean [see, e.g., *Kudryavtsev et al.*, 2008, and corresponding references in that paper]. Following *Phillips* [1985], F_w^{wb} can be calculated via wind forcing as: $F_w^{wb}=\int c\hat{T}_w(k) d\ln k$. As already noticed, the wind energy transfer to breaking crests, F_s^{wb}, is comparable with F_w^{wb} and may enhance the TKE production. This term can be expressed via the AFS stress as: $F_s^{wb}=\int c\hat{T}_s(k) d\ln k$ [*Kukulka and Hara*, 2008a, 2008b]. Thus, the total production of TKE beneath the surface should be defined as the sum of a "standard" term describing impact of wave energy losses due to wave breaking and additional term describing transfer of wind energy received by short-living breaking crests to the upper layer:

$$F^{wb}=F_w^{wb}+F_s^{wb}$$
$$=\int c(\hat{T}_w+\hat{T}_s)\ln k$$

Although either of the terms depends on the length of breaking wave crests, their spectral behavior is quite different (see Figure 4). This fact leads to different contribution of each of the mechanism to the TKE production over the depth. Further discussion of the impact of breaking waves on the water turbulence is out of the scope of this paper.

Following *Phillips* [1985], $\Lambda(\boldsymbol{k})$, the total length of wave breaking fronts, relates to the overall energy dissipation, $D(\boldsymbol{k})$:

$$D(\boldsymbol{k}) \propto g^{-1}c^5\Lambda(\boldsymbol{k}) \tag{15}$$

with proportionality constant of order from $O(10^{-2})$ to $O(10^{-4})$ [e.g., *Romero et al*., 2012; *Kleiss and Melville*, 2010, for more details and references). In the present coupled model, the energy dissipation is defined by the second term in (A1): $D=\alpha g^{-1}c^5k^{-1}(B/\alpha)^{n+1}$. Comparing this relation with (15) we have:

$$\begin{aligned}\Lambda(\boldsymbol{k}) &= k^{-1}[B(\boldsymbol{k})/\alpha]^{n+1}\\ &= \alpha^{-1}k^{-1}\beta(\boldsymbol{k})B(\boldsymbol{k})\end{aligned} \tag{16}$$

The second relation in (16) implies that wind forcing and dissipation in gravity range are the dominant terms in the energy balance equation (A1). In the gravity range of the wave spectrum $\alpha=2.8\times10^{-3}$ that fits into the range of expected values of proportionality constant in (15). Combining (3) and (16) gives:

$$\Lambda(\boldsymbol{k})=(c_\beta/\alpha)\hat{\tau}_l(u_*^2/g)\cos^2\varphi B(\boldsymbol{k}) \tag{17}$$

and the AFS force (7) can be rewritten as

$$\begin{aligned}zT_s(z) &= \hat{T}_s(k)_{k=\varepsilon_b/z}\\ \hat{T}_s(k) &= c_s\tau_l(u_b/c-1)^2B_0(k)\end{aligned} \tag{18}$$

where $c_s=2c_{db}\varepsilon_b c_\beta\alpha^{-1}f_\Delta(k/k_{mb})\int b_\varphi\cos^5\varphi d\varphi$ is the AFS stress parameter absorbing other parameters and integral angular property of $\Lambda(\boldsymbol{k})$. The function $f_\Delta(k/k_{bm})$ included in c_s restricts the existence of the AFS in the wave number range (k_{bm} is wave number of shortest breaking waves providing AFS). Indeed, small-scale breaking waves with $k > k_{bm}$ tend to generate parasitic capillaries spread over their forward slopes [*Longuet-Higgins*, 1963; *Fedorov et al*., 1998]. The generation of parasitic capillaries prevents the formation of sharp surface slopes, and thus prevents AFS over these waves. Generation of parasitic capillaries is included in the wave spectrum model (see relation (A8) with (A4) in Appendix A), and the form drag supported by these parasitic capillaries can be treated within the wave-induced stress defined by (2). Equation (18) provides a smooth transition from aerodynamically rough breaking crests and the form drag supported by AFS from crests of breaking waves with $k_b < k_{bm}$ to aerodynamically "smooth" regime and the form drag supported by momentum flux to parasitic capillaries generated by breaking waves with $k_b > k_{bm}$. In order to be consistent with the wave spectrum model, f_Δ is defined as: $f_\Delta(k/k_{bm})=1-f=\left[1+(k/k_{bm})^4\right]^{-1}$ with $k_{bm}=k_\gamma/4$, where f is the spectrum function defined by (A10) in Appendix A.

3.2. Turbulent Closure

For the turbulent closure, a simplified Kolmogorov-Prandtl closure scheme is adopted. The turbulent stress, τ, relates to the wind velocity gradient via turbulent eddy viscosity $k_t=lq^{1/2}$ as $\tau=k_t\partial u/\partial z$, where u is the mean wind velocity, q is the turbulent kinetic energy (TKE), l is the mixing length, and the TKE dissipation rate is $\varepsilon_t=q^{3/2}l^{-1}$. For the atmospheric boundary layer over the nonbreaking surface, the TKE balance equation reads [e.g., *Makin and Mastenbroek*, 1996, for more details):

$$(\tau+\tau_w)\partial u/\partial z-q^{3/2}l^{-1}=0 \tag{19}$$

In this equation, contributions of divergence of vertical turbulent transport of both the TKE and the wave-induced energy are omitted. The latter simplification is valid for "slow" (relative to the wind speed) surface waves, and loses its validity for fast surface waves (swell) where divergence of the wave-induced energy

flux dominates the TKE balance [e.g., *Kudryavtsev and Makin*, 2004]. Anticipating that most of the form drag, including wave breaking, is supported by "slow" surface waves, we use (19) in this study.

Wave breakings modify the TKE balance as argued by *Kukulka et al.* [2007] and recently demonstrated by *Suzuki et al.* [2013] using LES simulations. *Suzuki et al.* [2013] have found that TKE in the presence of breaking waves results from the balance of dissipation, shear production, and so-called wake production. The role of the vertical turbulent transport of TKE is weak. In the present model, accounting for the wake production is equivalent to adding the AFS stress to the wave-induced stress in the first term of (19). Solution of (19) accounting for the momentum balance (11) (with turbulent stress defined by $\tau=lq^{1/2}\partial u/\partial z$) reads:

$$q=u_*\left(u_*^2-\tau_w-\tau_s\right)^{1/2} \tag{20}$$

and the turbulent eddy viscosity and the turbulent stress are expressed as:

$$\begin{aligned} k_t&=\kappa(z+z_{0v})u_*\left[1-(\tau_w+\tau_s)/u_*^2\right]^{1/4}\\ \left(\frac{\tau}{u_*^2}\right)^{3/4}&=\frac{\kappa(z+z_{0v})}{u_*}\frac{\partial u}{\partial z}\end{aligned} \tag{21}$$

where we assumed that the mixing length is parameterized as $l=\kappa(z_0+z)$, $z_{0v}=c_v\nu/\tau_0^{1/2}$ is the viscous roughness length, $\tau_0=\tau(0)$ is the surface shear stress, ν is the kinematic viscosity in the air, $c_v\approx 0.1$ is a constant. If the form stress vanishes, $\tau_w+\tau_s=0$, equation (21) turns into the classical relation for the wall boundary layer. The water surface in (21) is treated as a smooth surface with the aerodynamic roughness $z_{0v}=c_v\nu/\tau_0^{1/2}$ scaled by viscous sublayer thickness (while the sea surface is of course aerodynamically rough due to the form drag supported by waves). Within this closure framework, the turbulent heat transfer coefficient, k_θ, and heat flux, Q, are parameterized as:

$$\begin{aligned} k_\theta&=\mathrm{Pr}^{-1}k_t\\ Q&=-\mathrm{Pr}^{-1}k_t\partial\theta/\partial z\end{aligned} \tag{22}$$

where Pr = 0.85 is the Prandl number [*Donelan*, 1990].

3.3. Solution

3.3.1. Momentum

Using (9) and (18), equation (10) takes the form:

$$\frac{\partial\tau}{\partial z}-\frac{\tau}{z}F(z)=0 \tag{23}$$

where F is a dimensionless function of the form drag:

$$F(z)=\left[c_wB_0(k)\right]_{k=\varepsilon_l/z}+r\left[c_s(U_{l_b}/c-1)^2B_0(k)\right]_{k=\varepsilon_b/z} \tag{24}$$

and $r=\tau(z\varepsilon_l/\varepsilon_b)/\tau(z)$ is a factor close to 1. Solution of this equation satisfying the boundary condition $\tau=u_*^2$ at large z ($z\to\infty$) is:

$$\tau(z)=u_*^2\exp\left(-\int_z^\infty F d\ln z\right) \tag{25}$$

Then the local coupling parameter $\alpha_c(z)=[\tau_w(z)+\tau_s(z)]/u_*^2$ is:

$$\alpha_c(z)=1-\exp\left(-\int_z^\infty F d\ln z\right) \tag{26}$$

Using the closure scheme (21), the vertical wind profile reads

$$u(z)=(u_*/\kappa)\int_0^z(\tau/u_*^2)^{3/4}(1+z_{0v}/z)^{-1}d\ln z \tag{27}$$

The resistance law defining the friction velocity u_* in the core of the boundary layer, well above the surface, as a function of the wind speed $U_h=u(h)$ at reference level $z=h$, the surface drag coefficient, C_{Dh}, becomes:

$$\begin{gathered}u_*^2=C_{Dh}U_h^2\\ C_{Dh}=\left[\kappa/\int_0^h(\tau/u_*^2)^{3/4}(1+z_{0v}/z)^{-1}d\ln z\right]^2\end{gathered} \tag{28}$$

substituting $\tau(z)$ from (25) gives:

$$C_{Dh}=\left[\kappa/\int_0^h\exp\left(-3/4\int_z^\infty F d\ln z\right)(1+z_{0v}/z)^{-1}d\ln z\right]^2 \tag{29}$$

If $F\equiv 0$, then (27) corresponds to the classical drag coefficient for the smooth surface. Wind waves extract momentum from the airflow leading to transition of the sea surface from aerodynamically smooth to rough. The impact of wave breaking on the surface drag increases faster with wind speed than that of nonbreaking waves, compare the first and the second terms in the RHS of (24). Therefore, we may anticipate that at high winds the form drag of the sea surface is mainly supported by breaking waves.

3.3.2. Heat

At stationary conditions, the component of the heat flux from the wave-induced oscillations is negligible, and the heat balance in the lower part of the atmospheric boundary layer above waves is reduced to the height independent turbulent heat flux: $Q(z)=const$ [*Makin and Mastenbroek*, 1996]. Using (22) with eddy viscosity (21), the air temperature profile takes the form:

$$\theta(z)=\theta_s-\mathrm{Pr}\,Q/(\kappa u_*)\int_0^z(\tau/u_*^2)^{-1/4}(1+z_{0v}/z)^{-1}d\ln z \tag{30}$$

where θ_s is the water temperature. Correspondingly, the heat transfer coefficient, C_{Qh}, relates the heat flux to the wind speed, U_h, and the air temperature, θ_h, at reference level $z=h$ as:

$$Q=C_{Qh}(\theta_s-\theta_h)U_h \tag{31}$$

Using (30), it reads:

$$\begin{gathered}C_{Qh}=c_\theta^{1/2}C_{Dh}^{1/2}\\ c_\theta^{1/2}=\mathrm{Pr}^{-1}\frac{\kappa}{\int_0^h(\tau/u_*^2)^{-1/4}(1+z_{0v}/z)^{-1}d\ln z}\end{gathered} \tag{32}$$

A reduction of the turbulent stress near the surface, or an increase of the coupling parameter (since $\tau/u_*^2=1-\alpha_c$) decreases the temperature gradient in the core of the boundary layer, thus decreasing the heat transfer coefficient (32). On the other hand, the same effect works opposite way by increasing the drag coefficient (see (28)), and thus the heat transfer coefficient. Overall, the wind wave coupling parameter impacts both, C_{Dh} (by increasing it) and $c_\theta^{1/2}$ (by decreasing it) leading to overall weak dependence of the heat transfer coefficient C_{Qh} on wind speed. Notice that (31) and (32) can be used for any scalar quantity, e.g., the water vapor humidity.

4. Results

Given the wind speed at a reference level, the wind wave coupled model consist of the closed system of algebraic equations describing wave spectrum (relation (A12) with (A7) and (A8)), drag coefficient (28), vertical profile of the shear stress (25), and the wind velocity (27). Solution of this system of equations can be

found by iterations. Once solution has found, the heat transfer coefficient (32), temperature profile (30), as well as other parameters of the sea surface (e.g., MSS, (33), and length of breaking crests, (17)) can easily be calculated.

Parameters of the wave spectrum model are constrained by observations [*Yurovskaya et al*., 2013] and kept unchanged. Next, we focus on remaining tuning parameters to match the fully coupled model to observations. These remaining parameters are included in the parameterization of the AFS stress (18), leaving very little "freedom" to adjust them given that the length of breaking crest, $\Lambda(\boldsymbol{k})$, is already predefined by the spectral model.

4.1. Nonbreaking Surface

Let us first consider the coupled model prediction when the wave breaking stress is "switched off." In this case, all parameters of the coupled model are set, and the same growth rate (3) governs both the water- and the air-side of the coupled model. The drag coefficient and the Charnock parameter for this truncated variant of the coupled model are shown in Figure 1. Figure 2 illustrates the mean square slope (MSS) of the sea surface

$$s^2 = \int\int B(\boldsymbol{k}) d\varphi d\ln k \tag{33}$$

and its cross-wind, s^2_{cr}, and up-wind, s^2_{up},

$$\begin{aligned} s^2_{cr} &= \int\int \sin^2\varphi B(\boldsymbol{k}) d\varphi d\ln k \\ s^2_{up} &= \int\int \cos^2\varphi B(\boldsymbol{k}) d\varphi d\ln k \end{aligned} \tag{34}$$

where $\varphi = 0$ corresponds to the wind direction. Referring to Figure 2, the model MSS is apparently consistent with *Cox and Munk*'s [1954] field data. Given reasonable MSS, together with reasonable magnitude of the wind wave growth rate, the sea surface drag coefficient is expected to be in close agreement with empirical values. But this is not the case, and the model drag coefficient and the Charnock parameter are apparently underestimate data by *Fairall et al*. [2003] and *Edson et al*. [2013] obtained in field conditions (Figure 1).

We further check if the truncated (without AFS) model is capable to reproduce the data with enhanced spectrum level. Figure 1 shows model drag coefficient with an MSS increased twofold (via a twofold increase of the spectrum level). In this case, C_{D10} becomes comparable with the measurements at high winds, but it overestimates the data at low winds. The Charnock constant, Figure 1b, demonstrates more evidently the inability of a truncated model to reproduce the data (even with unrealistically large MSS), especially to reproduce the observed wind trend in $z_0 g/u_*^2$. Notice that calculations in Figures 1a and 1b are similar to results by *Chalikov and Rainchik* [2010, Figures 10 and 11]. In order to reproduce observed C_{D10}, *Chalikov and Rainchik* [2010] assumed the spectrum tail in the wave number range up to shortest scales (and thus MSS) to depend on wave-age. Such an assumption, never been strongly supported in real sea conditions, led to results similar to the truncated model contradicting to the observations.

4.2. Impact of Wave Breaking

As the length of wave breaking crests is also prescribed by the spectral model, the remaining tuning parameters in the definition of the AFS stress are the local drag coefficient of an individual breaking crest, c_{db}, and the steepness, ε_b, of breaking waves. The latter varies between 0.3 and 0.5. Following an analogy of a breaking crest with a backward step, an empirical value of c_{db} can vary between 0.1 and 0.5 [see discussion in *Kudryavtsev and Makin*, 2001].

The drag coefficient and the Charnock parameter for the full coupled model are shown in Figure 1. Inclusion of the AFS stress results in better match of the model form drag with the *Fairall et al*. [2003] measurements. It also reproduces the wind dependence of the Charnock parameter. The best fit to observations is found at $c_{db} = 0.35$ and $\varepsilon_b = 0.3$. As expected, the impact of the breaking stress is negligible at low winds. But it becomes increasingly important at stronger winds where it grows faster than nonbreaking wave-induced

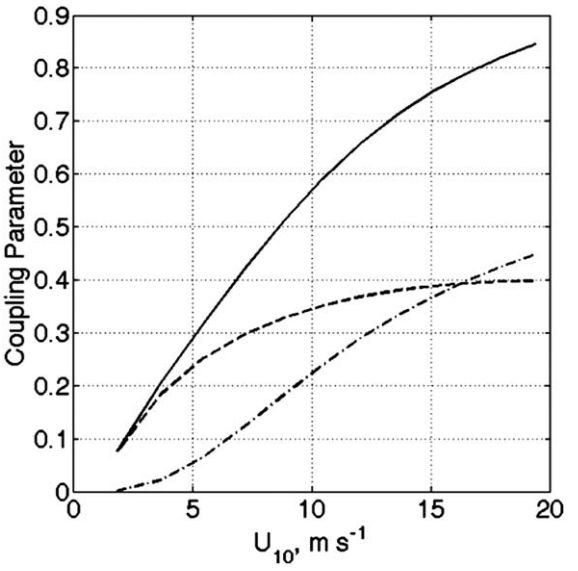

Figure 3. Wave-induced stress τ_w/u_*^2 (dash line), wave breaking stress τ_s/u_*^2 (dash-dotted line, and their sum (solid lines) scaled by the square friction velocity as a function of wind speed.

stress (Figure 3). At wind speeds above 15 m/s, the wave breaking contribution to the form drag exceeds the contribution of nonbreaking waves.

Spectral behavior of the wave-induced and the wave breaking stresses is shown in Figure 4. The spectral contribution of wind waves to wave-induced stress is almost uniform, similar to what has been previously reported by *Kudryavtsev and Makin* [1999]. The bulk impact of breaking stress is dominated by the shortest waves (see Figure 4). This is explained by the spectral distribution of the length of wave breaking fronts, $\Lambda(\boldsymbol{k})$. Following (17), the contribution of the spectral peak breaking waves is relatively modest. This has been experimentally verified by *Gemmrich et al*. [2008] and *Sutherland and Melville* [2013, Figure 1]; see also Figure 6, for comparison. The spectral distribution of the total stress shown in Figure 4, indicates that the surface drag is mainly supported by the form drag corresponding to the high-frequency tail of the wind wave spectrum.

Momentum flux to the "regular" and breaking waves results in significant deviation of the vertical wind profile from the reference one corresponding to the airflow over the smooth (no impact of waves) surface (Figure 5). This deviation can be treated as a deceleration of the airflow due to the sheltering, which is mostly controlled by wave breakings.

4.3. Sea Surface Properties

The most remarkable feature of simulated wave spectra is a strong sensitivity of the energy of centimeter-to-millimeter waves to the wind speed (Figure 6). At moderate winds, a clear spectral peak of the saturation spectrum is present in the millimeter wavelength range. This peak

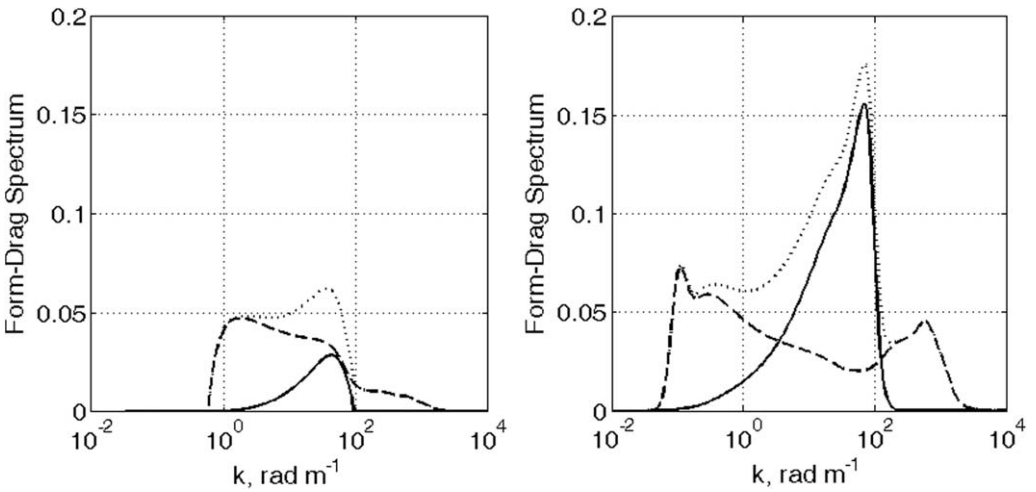

Figure 4. Spectra of the wave-induced (dash lines) and wave breaking (solid lines) stresses at the surface and their sum (dotted lines) at (left) 5 m/s and (right) 15 m/s.

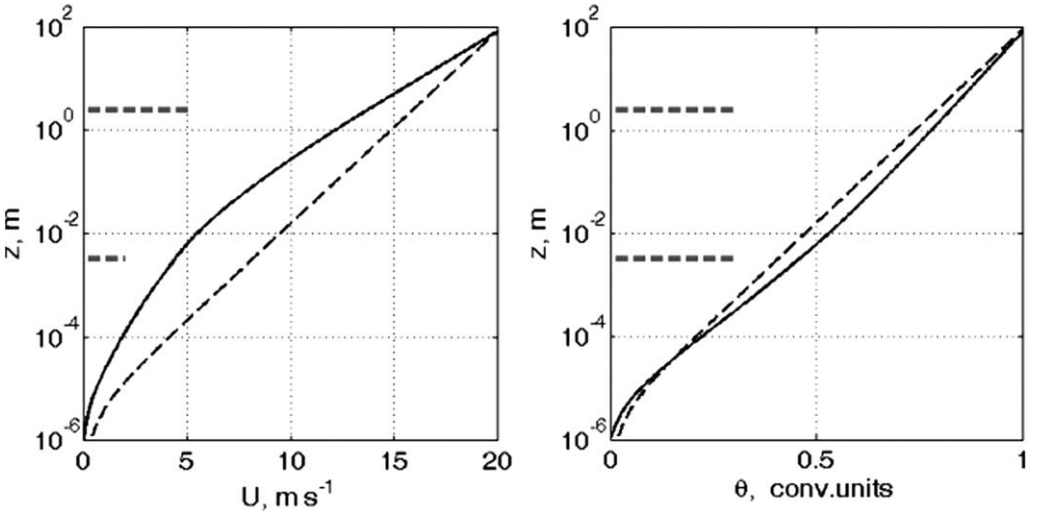

Figure 5. (left) The wind and (right) the air temperature profiles at 20 m/s wind speed at reference level $z = 100$ m. Dash lines show "reference" profiles when form drag is switched off (aerodynamically smooth surface). Solid lines show the full model calculations. Gray dash lines adjacent to the z axis indicate altitude of the impact of spectral peak wave (top line) and shortest breaking waves (bottom line) on the form stress.

corresponds to generation of the parasitic capillaries. Simulated spectra of shortwaves are consistent with observations. Interested readers are referred to *Yurovskaya et al*. [2013] for more extensive comparisons with measurements.

Model $\Lambda(\boldsymbol{k})$ (defined by (17) but transformed to 1-D distribution $\Lambda(c)$) in Figure 6 is consistent with the *Sutherland and Melville* [2013] measurements that include observations of breaking crests with and without white caps as well as breaking crests generating parasitic capillaries. Sharp fall of observed $\Lambda(c)$ toward large spatial scales suggests the dominant contribution of the shortest breaking waves to the form drag of the surface.

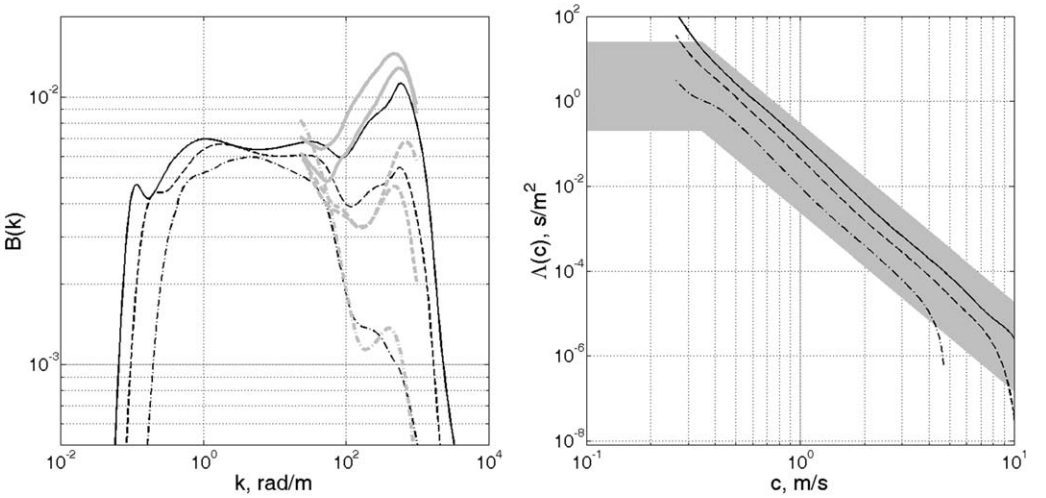

Figure 6. (left) Omnidirectional saturation spectra of wind waves at 100 km fetch. Black lines are model calculations at wind speeds 5 m/s (dash-dotted lines), 10 m/s (dash lines), and 15 m/s (solid lines). Gray lines are measurements by *Yurovskaya et al*. [2013] at 4.6 m/s (dash-dot), 10.3 m/s and 10.2 m/s (dash), and 14.4 and 15.9 m/s (solid). (right) Omnidirectional length of breaking front versus phase speed of breaking waves at 100 km fetch. Black lines show model $\Lambda(c)=(2k/c)\Lambda(k)$ with $\Lambda(k)$ defined by (17) at (dash-dot) 5 m/s, (dash) 10 m/s, and (solid) 15 m/s (corresponding inverse wave-age, U_{10}/c, is 0.84, 1.13, and 1.43). Shaded area schematically indicates measured $\Lambda(c)$ presented by *Sutherland and Melville* [2013, Figure 1].

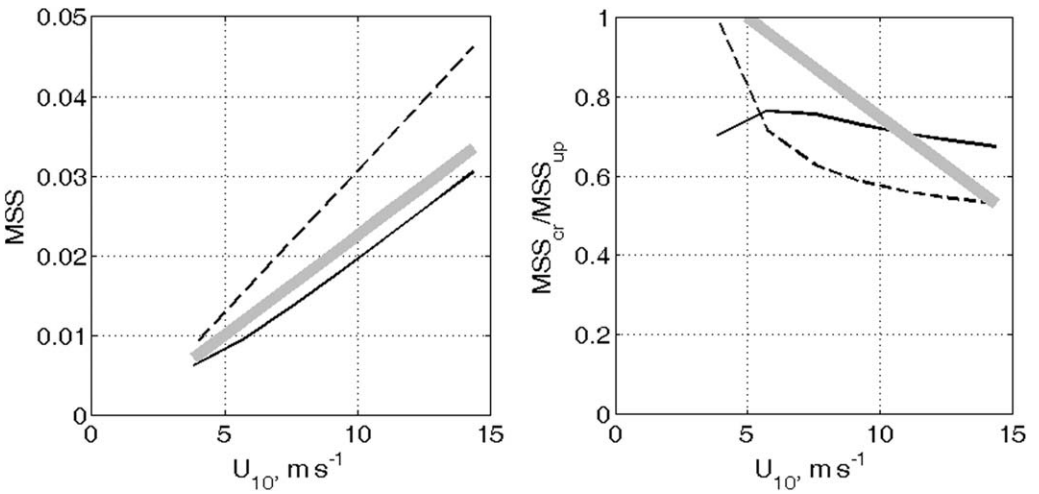

Figure 7. (left) The mean square slope (MSS) of the sea surface in the wave number interval $k > 20$ rad/s and (right) ratio of the cross-wind to the up-wind components of the MSS versus wind speed: dash lines are *Cox and Munk* [1954] data defined as a difference between MSS for the clean and slick surface; solid lines are the model calculations; gray solid lines are fit of the measurements by *Yurovskaya et al*. [2013].

MSS growth with the wind is apparently reduced at winds above 10 m/s (Figure 2), which is a consequence of a sheltering of shortwaves by larger scale waves. The model short-wave MSS (integrated over $k > 20$ rad/m, Figure 7) is consistent with observations. Observed MSS of shortwaves is estimated from the *Cox and Munk* [1954] data as the difference between MSS of the clean surface and MSS of the slick covered surface [*Vandemark et al*., 2004]. Although it is difficult to estimate the exact spectral interval of waves suppressed in natural slicks, we here adopt that waves shorter than 30 cm are effectively suppressed, as discussed by *Cox and Munk* [1954].

4.4. Heat Transfer

The impact of wind waves on the air temperature profile and the heat transfer coefficient is very different from its impact on the wind and form drag. Referring to Figure 5, we see that effect of waves on the temperature profile acts in the opposite direction, as compared to the wind profile. It leads to relative decrease of the air temperature gradient above the layer affected by waves. This is an apparent consequence of the reduction of turbulent eddy viscosity in the sheltered layer near the surface. Indeed, to maintain the heat flux constant, the temperature gradient in the sheltered layer increases that results in decrease of its value in the layer above.

Model heat transfer coefficient, relation (32), and the roughness scale, z_{0t} for temperature defined as:

$$z_{0t} = h\exp\left(-\kappa c_{\theta}^{-1/2}\right) \tag{35}$$

are shown in Figure 8. In the presence of waves, the roughness scale z_{0t} drops relative to its value over smooth surface. In contrast, the heat transfer coefficient for the full model exceeds the values corresponding to the smooth surface. The enhanced momentum roughness scale overcomes the effect of decreasing the temperature roughness scale, thus the net wave impact results in increasing heat transfer coefficient with wind.

The *Fairall et al*. [2003] empirical heat transfer coefficient

$$C_{H10} = \kappa^2/[\ln(10/z_0)\ln(10/z_{0t})] \tag{36}$$

and the temperature roughness scale

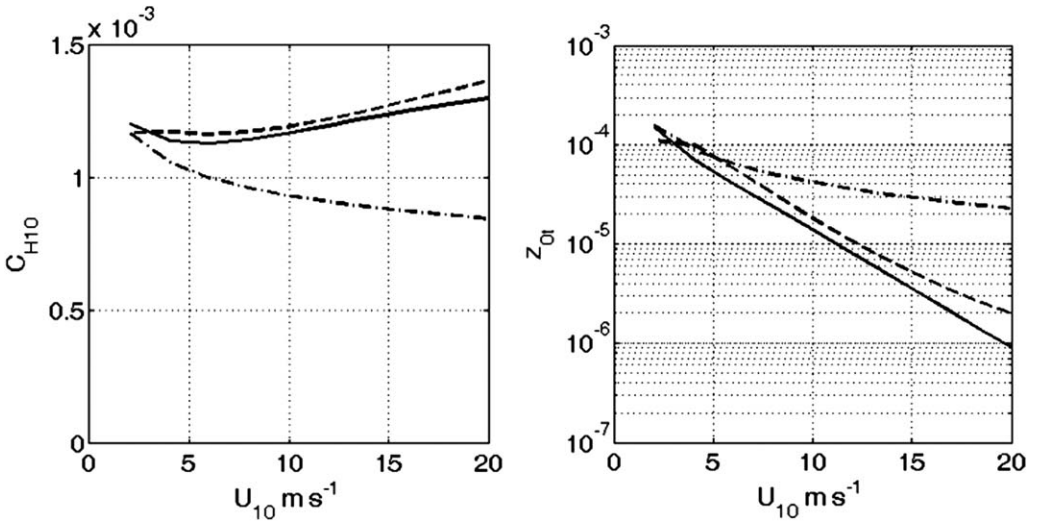

Figure 8. (left) Heat transfer coefficient and (right) the heat transfer roughness scale versus wind speed: dash lines show empirical dependences suggested by *Fairall et al*. [2003], COARE 3.0 data; dash-dotted lines are the heat transfer relations for the smooth surface (form drag is switched off); solid lines are the model calculations following (32) and (35).

$$z_{0t}=\min\left[1.1\times10^{-4},\,5.5\times10^{-5}(z_0u_*/\nu)^{-0.6}\right] \tag{37}$$

are also included in Figure 8 for the reference. The model is in close agreement with empirical data reproducing both momentum and heat transfer characteristics.

5. Discussion

5.1. Sensitivity of Drag Coefficient to Wave Spectrum Variations

We remind that the "water-side" of the coupled model is constrained by the measurements (*Yurovskaya et al*. [2013], for short-wave spectrum; *Donelan et al*. [1985], for dominant wave spectrum; *Cox and Munk* [1954], for the MSS; *Sutherland and Melville* [2013], for breaking crests length) and does not possess any free tuning constants. On the other hand, one may anticipate that these measurements describe some averaged statistical properties of the sea surface, and in reality wave spectrum (as well as wave breaking) may significantly vary relative to this mean state.

The linear response of the drag coefficient (29) to variations, δF, of the form drag function (24), is described by

$$\frac{\delta C_{Dh}}{C_{Dh}}=\frac{3}{2}\frac{\int_0^h\left(1+z_{0v}/z\right)^{-1}\left(\tau/u_*^2\right)^{3/4}\int_z^\infty \delta F d\varsigma' d\varsigma}{\int_0^h\left(1+z_{0v}/z\right)^{-1}\left(\tau/u_*^2\right)^{3/4}d\varsigma} \tag{38}$$

where δC_{Dh} is deviation of the drag coefficient from its "undisturbed" value caused by δF. Let us assess impact of wave spectrum variations specified as $\delta B=\gamma B$ (γ is a small constant) on drag coefficient. Following (24), variation of form drag function F in this case is $\delta F=\gamma F$. Response of the drag coefficient to the spectrum variations defined as $\delta C_{Dh}/(\gamma C_{Dh})$ is shown in Figure 9. Since impact of wind waves on the surface drag increases with the wind speed (see, e.g., Figure 3), sensitivity of the drag coefficient to variations in the wind wave spectrum also increases with increasing wind speed. Magnitude of the response coefficient is quite low, about 0.3–0.4 at wind speed around 10 m/s, therefore using linear relation (38) we may assess effect of rather "large" spectrum modulations on C_{Dh}. Referring to Figure 9, one may find that quite strong spectrum modulations, with $\gamma=\pm50\%$ result in weaker variations of the drag coefficient, about $\pm10\%$ to 25 % at wind speeds in the range from 5 to 20 m/s. If we assume that such spectral variations envelop natural

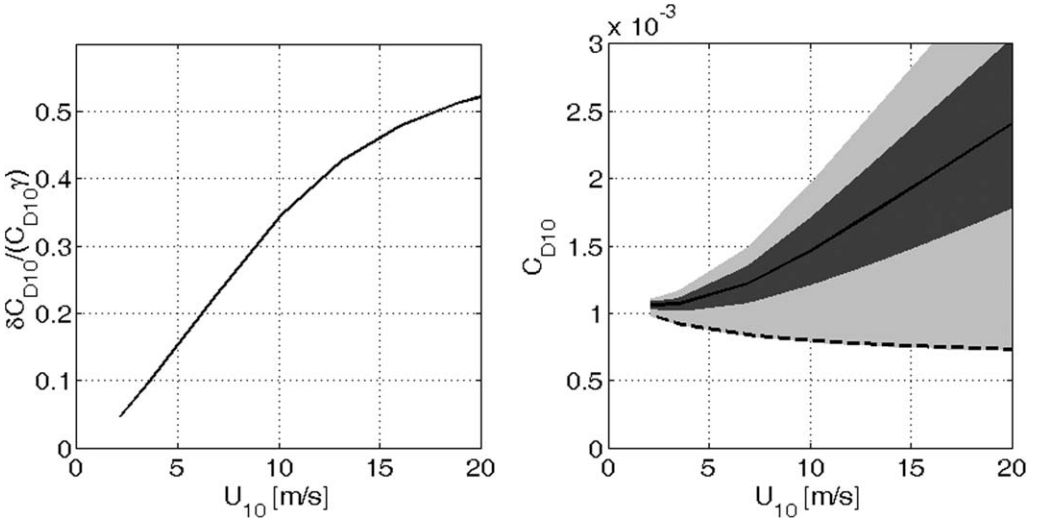

Figure 9. (left) Coefficient of sensitivity of the surface drag coefficient, $\delta C_{D10}/(\gamma C_{D10})$, to the wave spectrum variations, $\delta B=\gamma B$ versus wind speed. (right) Scattering of the model drag coefficient from the "undisturbed" values (solid line) caused by variations of the wave spectrum at different wind speeds. Upper and lower bounds of the dark shaded area correspond to the spectrum variations with $\gamma=0.5$ and $\gamma=-0.5$, respectively. Upper bound of the light shaded area corresponds to the spectrum variations with $\gamma=1.0$, and the lower bound corresponds to $\gamma=-1.0$. In the latter case, wave spectrum level vanishes, thus drag coefficient coincides with smooth surface drag coefficient shown by dash line.

variability of wave field (in the open sea conditions), then simulations shown in Figure 9 may explain reported scattering in measurements of C_{D10} [except for a low wind conditions when origin of scattering of C_{D10} measurements is different, see, e.g., *Edson et al*., 2013]. Range of C_{D10} variations for "maximum permissible" limit $\gamma=\pm100\%$ provides further insight in possible range of C_{D10} variability, Figure 9. Notice that use of linear relationship (38) for this case is questionable. Therefore, the low limit for C_{D10} at $\gamma=-1.0$ (spectrum level is vanished) is set on the drag coefficient for the smooth surface, thought the upper limit for C_{D10} at $\gamma=1.0$ is calculated following (38).

As a matter of fact, relationship (38) shall be useful for investigation of spatial variability in surface fluxes (momentum and heat) caused by interaction of wind waves with nonuniform surface currents, as well as suppression of shortwaves by surfactants in slicks. Following (38), modulations of wave spectrum and wave breaking should lead to variations in surface drag coefficient (as well as in the heat transfer coefficient), that may in turn engender a feedback between the atmosphere and the upper ocean boundary layers.

5.2. Alternative Description of AFS Stress

Model calculations demonstrate the crucial role of wave breaking contribution in supporting the air-sea fluxes. The AFS stress parameterization in the model is based on similarity of a breaking crest with a backward step. While being practical, this analogy can appear too restrictive to describe the complexity of wave breakings. Wave breakings are often accompanied with intense crest disruptions, development of egg-like roughness patterns that entrain the air and result in well-visible whitecaps.

Rather than being produced by wave breakings along sharp one-dimensional crests, experimental spectra of surface disturbances generated by breaking waves appear almost isotropic and fall off as roughly $k^{-3.5}$ at wave numbers above the spectral peak wave number [*Walker et al*., 1996; *Ericson et al*., 1999]. We suggest that such spectra can be treated as Kolmogorov-type spectra resulting from the energy flux, P, from the largest energetic breaking disturbances toward shorter scales. The energy flux is $P\propto gk_b^{-2}\omega_b=c_b^3$, where ω_b, k_b, and c_b are frequency, wave number, and phase velocity of the breaking wave. Hence, from dimensional analysis 2-D spectrum, $\Psi_b(\boldsymbol{k})$, of breaking crest roughness elevations is: $g\Psi_b(\boldsymbol{k})\propto P^{2/3}k^{-3}$. Corresponding 1-D spectrum, $\psi_b(k)$, reads:

$$\psi_b(k)=\gamma k_b^{-1}k^{-2} \tag{39}$$

where $\gamma \approx 7\times10^{-2}$ is a proportionality constant to fit data reported by *Ericson et al*. [1999, Plate 1]. From these measurements, the disturbance spectra peaked at wave number k_P, $k_P=pk_b$, with a parameter p varying in the range $p \approx 6-10$ depending on breaker intensity. The significant height of local roughness patches, h_b, corresponding to the spectrum (39) is:

$$h_b=4\left(\int_{k_P}^{k_c}\psi dk\right)^{1/2}\approx 4\gamma^{1/2}p^{-1/2}k_b^{-1} \tag{40}$$

At $p \simeq 6$, the steepness of the crest roughness is rather large, about $h_bk_P \approx 2.5$ (or $h_bk_b \approx 0.4$). Following *Melville* [1977], a local aerodynamic roughness scale, z_{0b}, provided by these rough and steep patches can be defined as:

$$z_{0b}=(1/m)h_b \approx 4m^{-1}\gamma^{1/2}p^{-1/2}k_b^{-1} \tag{41}$$

where m is an empirical constant of the order of O(1–10) [i.e., *Melville*, 1977]. We further assume that these aerodynamically rough patches cover a fraction of the sea surface proportional to $\propto k^{-1}\Lambda d\boldsymbol{k}$. Adjustment of the airflow to these abrupt changes in the surface roughness results in development of an inner boundary layer over each of these rough patches (to keep similarity in terminology, hereafter this internal boundary layer is referred to as the inner region, IR). Depth of this IR, l_b, is proportional to the distance from the windward edge of a patch: $\propto c_{db}^{1/2}x$ (c_{db} is the local drag coefficient). At the down-wind side of a patch, $x \propto k_b^{-1}$, the IR depth reaches the maximum:

$$l_b \approx c_{db}^{1/2}k_b^{-1} \tag{42}$$

This IR depth corresponds to the height of impact of wave breaking on the vertical profile of momentum flux (similar to the height, $\varepsilon_b k_b^{-1}$, of the "separation bubble" in (1); see also *Suzuki et al*. [2013] for the LES of airflow over an individual breaker).

As the airflow accelerates above wave crests, the wind speed on the upper boundary of the internal boundary layer, l_b, is presented as the sum of the mean wind speed and the wave-induced variations: $u_b=u_{l_b}+\varepsilon_b(u_{l_b}-c)$, where $u_{l_b}=u(l_b)$ [e.g., *Kudryavtsev and Makin*, 2004]. Turbulent stress within the IR, τ_b (which is equal to the surface stress acting on the breaking crest) is proportional to the squared velocity difference $\propto (u_b-c)^2$:

$$\tau_b=2c_{db}(u_{l_b}-c)^2 \tag{43}$$

where $(1+\varepsilon_b)^2 \approx 2$, and c_{db} is the surface drag coefficient for the IR defined as:

$$c_{db}=\kappa^2/\ln^2(l_b/z_{0b}) \tag{44}$$

Accounting for the breaking crests roughness scale (41), the local drag coefficient (44) becomes:

$$c_{db}=\kappa^2/\ln^2\left(1/4\cdot c_{db}^{1/2}m\gamma^{-1/2}p^{1/2}\right) \tag{45}$$

At $\gamma=7\times10^{-2}$, $m=5$, and $p=6$ the drag coefficient for breaking crests is $c_{db} \approx 10^{-1}$.

To account for average drag imposed by wave breakings, τ_b is further normalized by the fraction of the sea surface covered by enhanced roughness patches generated by breaking crests. For a narrow spectral band, the fraction is proportional to $\propto k^{-1}\Lambda d\boldsymbol{k}$ with a proportionality constant α_b of the order of O(1). Thus, the stress supported by all breaking crests reads:

$$\begin{aligned} d\tau_s&=\alpha_b\tau_b k^{-1}\Lambda d\boldsymbol{k}\\ &=2\alpha_b c_{db}(u_{l_b}-c)^2k^{-1}\Lambda d\boldsymbol{k}\end{aligned} \tag{46}$$

It is not surprising to see, strong similarity between (4) and (46). In both cases, the overall impact of breaking waves on the surface drag is proportional to their intensity (expressed in terms of total length of

breaking fronts), and the form drag of individual breakers varies as wind speed squared (from dimensional reasons). Accordingly, the two mechanisms can possibly coexist. Yet, the mechanism associated with breaking crest disruptions may be suggested to be closer to visual observations and experimentally measured intense near-isotropic roughness changes at the crest and roughness patches in the wake of larger scale breakers.

6. Conclusions

Following previous attempts, a revised wind-over-wave-coupling model is suggested. A consistent description of the coupled wind wave system is derived to provide the form drag and heat/moister transfer coefficients, wind velocity profiles, wind wave spectra in the decimeter to millimeter wavelengths, and wave breaking parameters. A key role in this new development is related to the overall impact associated with local and intermittent wave breakings. Wave breakings control energy losses from the gravity waves, generate shorter surface waves including parasitic capillaries, and support a significant portion of the surface form drag. The present model describes a transition between aerodynamic properties of breaking crests from aerodynamically "rough," with a local form drag supported by the AFS, to aerodynamically "smooth," with a form drag supported by momentum flux to parasitic capillaries.

Wave spectrum in the coupled model is represented as a solution of the wave action budget equation. The terms of this equation are constrained to reproduce the fundamental statistical properties of the sea surface including the mean square slope and the spectral density of breaking crest lengths. They are also fit to reproduce in situ instrumental measurements of short wind wave spectra [*Yurovskaya et al*., 2013]. In that sense the "water-side" part of the model does not include any free tuning parameters. The "air-side" of the model has only one tuning parameter, the form drag coefficient of a breaking crest that is adjusted to match with experimental data.

The form drag of the sea surface cannot be explained solely by considering interactions between the airflow and the regular (nonbreaking) surface. Introduction of the form drag supported by wave breaking crests helps to reconcile the model surface drag with observations. The form drag supported by wave breakings rapidly increase with wind speed. Its contribution to the form drag exceeds that of the regular nonbreaking waves at winds above 15 m/s.

The impact of wind waves on the air temperature profile and the heat transfer coefficient is different from their impact on the momentum characteristics. Due to the suppression of the turbulent mixing in the sheltered layer near the surface, the temperature gradient in this layer increases to maintain the heat flux constant. This in turn leads to decrease of the temperature gradient in the layer above. This deformation of the vertical temperature profile tends to lower the temperature roughness scale compared to its value over the smooth surface.

Simulated momentum and heat transfer characteristics as well as the sea surface properties agree with available experimental data, suggesting that this semiempirical coupled model may serve as a simple practical tool for investigations of various aspects of the air-sea interactions and remote sensing issues.

Appendix A: Wave Spectrum

Model of the wind wave spectrum suggested in *Kudryavtsev et al*. [1999] and *Kudryavtsev and Johannessen* [2004] and recently constrained using *Yurovskaya et al*. [2013] data are used. In order to emphasize the strong link between "water-side" and "air-side" of the coupled model, we give below a brief overview of the spectrum model.

Shape of the spectrum results from solution of the energy balance equation

$$Q(B) \equiv \omega^3 k^{-5}\left[\beta_v(\boldsymbol{k})B(\boldsymbol{k}) - B(\boldsymbol{k})\left(\frac{B(\boldsymbol{k})}{\alpha}\right)^n + Q_b(\boldsymbol{k})\right] = 0 \tag{A1}$$

where $Q(B)$ is the total energy source consisting of (the first term) effective wind forcing, (the second term) nonlinear energy losses (associated with wave breaking in the gravity range, and nonlinear limitation of the

spectral level in the capillary-gravity range), and (the third term) generation of shortwaves by breaking of longer waves (Q_b), including generation of parasitic capillaries. In this equation, $\beta_v(\mathbf{k})=\beta(\mathbf{k})-4\nu k^2/\omega$ is the effective growth rate, which is the difference between the wind growth rate $\beta(\mathbf{k})$ and viscous dissipation (ν is water viscosity coefficient). Wind growth rate in the spectrum model is defined by the same relation (3) as in wave-induced momentum flux. Parameters α and n in (A1) are tuning functions, which are equal to constants $\alpha=\alpha_g, n=n_g$ at $k/k_\gamma \ll 1$, and equal to other constants (e.g., $n=1$) at $k/k_\gamma \approx 1$, $k_\gamma=(g/\gamma)^{1/2}$ is wave number of minimum phase velocity.

Source term $Q_b=Q_b^{pc}+Q_b^w$ describes generation of short surface waves by wave breaking. As suggested, breaking crests of waves with $k \le k_{bm}$ generate enhanced surface disturbances characterized by spectrum (39). Once breaking process is completed, these surface disturbances disperse and generate "freely" propagating angularly isotropic surface waves. Rate of their generation is defined by see *Kudryavtsev and Johannessen* [2004, for more details]:

$$\omega k^{-4} Q_b^w(k) \propto k^{-3} \int_0^{\min(k/p,k_{bm})} k_b^{-1} c_b \Lambda(\boldsymbol{k}_b) d\boldsymbol{k}_b \tag{A2}$$

Notice that this equation differs from *Kudryavtsev and Johannessen* [2004], their equation (9), due to introduction of another spectrum (39) for the breaking crest roughness. With use of (16), relation (A2) becomes

$$Q_b^w(k)=c_b^w c^{-1} \int\int_0^{\min(k/p,k_{bm})} c\beta B d\varphi d\ln k \tag{A3}$$

where c_b^w is a tuning constant, here $c_b^w=2.7\times10^{-2}$, chosen so that to fit observed level of short-wave spectrum at cross-wind directions [see *Yurovskaya et al*., 2013, for more explanation].

Due to the effect of the surface tension, breaking waves with $k > k_{bm}$ are not disrupted, but produce "regular" trains of parasitic capillaries. Wave numbers of generated capillaries, k, and breaking waves, k_b, are linked as: $kk_b=k_\gamma^2$. Rate of generation of parasitic capillaries is:

$$Q_b^{pc}(\boldsymbol{k})=\phi(k)[\beta B]_{k_b=k_\gamma^2/k} \tag{A4}$$

where $\phi(k)$ is a filter function restricting generation of parasitic capillaries in k-space.

It is assumed that the spectrum of shortwaves (waves from the equilibrium range), B_{sw}, is a superposition of spectrum of "freely propagating" surface waves generated by wind forcing and wave breaking (we call them as wind waves), B_w, and spectrum of parasitic capillaries (bound waves), B_{pc}, generated on the crests of that freely propagating waves:

$$B_{sw}(\boldsymbol{k})=B_w(\boldsymbol{k})+B_{pc}(\boldsymbol{k}) \tag{A5}$$

Either $B_w(\boldsymbol{k})$ and $B_{pc}(\boldsymbol{k})$ spectra are defined as solution of the energy balance equation (A1). Spectrum B_w is found as solution of (A1) where Q_b is replaced by Q_b^w. Solution of such a nonlinear equation is not straightforward, but it can be effectively found by iterations starting from approximate solutions for up-, down-, and cross-wind directions. At down-wind directions source Q_b^w should be small relative to wind forcing, and approximate solution of (A1) is: $B_w^d=\alpha\beta_v^{1/n}$. At cross-wind directions $\beta_v \approx 0$, and we have: $B_w^{cr} \approx \alpha^{n/(n+1)}\left(Q_b^w\right)^{1/(n+1)}$. Finally, at up-wind directions (where $\beta_v(\boldsymbol{k}) < 0$), the spectral level is small enough to ignore nonlinear term, thus: $B_w^{up} \approx -I_{wb}/\beta_v$. Combination of these three "asymptotic" solutions

$$B_w^0=\max\left[B_w^d, \min\left(B_w^{cr}, B_w^{up}\right)\right] \tag{A6}$$

provides a first guess for wave spectrum. Next iteration for wave spectrum is defined by

$$B_w^j=B_w^{j-1}-[Q(B_w)/(\partial Q/\partial B_w)]_{B_w=B_w^{j-1}} \tag{A7}$$

Practically, iteration scheme (A7) with the first-guess (A6) converges after three iterations.

Spectrum of parasitic capillaries results from the same energy balance equation (A1) where the parasitic capillary term $Q_b = Q_b^{pc}$ is the only energy source (wind forcing is omitted). Solution of this equation is straightforward and reads:

$$B_{pc}(\boldsymbol{k}) = \frac{\alpha}{2}\left[-4\nu k^2/\omega + \sqrt{(4\nu k^2/\omega)^2 + 4Q_b^{pc}(\boldsymbol{k})/\alpha}\right] \tag{A8}$$

with Q_b^{pc} defined by (A4) with B replaced by B_w.

The model tuning functions $n(k/k_\gamma)$ and $\alpha(k/k_\gamma)$ are defined following *Kudryavtsev et al*. [2003], and specified as

$$\begin{aligned} 1/n(k) &= (1-1/n_g) f(k/k_{bm}) + 1/n_g \\ \ln[\alpha(k)] &= \ln a - \ln \bar{c}_\beta / n \end{aligned} \tag{A9}$$

with $\overline{c_\beta} = 0.03$ as a mean value of the growth rate, parameter n_g is fixed at $n_g = 10$ in order to be consistent with *Banner et al*. [1989] data. Tuning function $f(k/k_{bm})$ in (A9) is specified as

$$f(x) = x^4/(1+x^4) \tag{A10}$$

with k_{bm} equal to $k_{bm} = 1/4k_\gamma$, – is wave number dividing breaking waves on large-scale breaking waves (with $k < k_{mb}$), which generate the crest's perturbations with spectrum (39), and small-scale breaking waves (with $k > k_{mb}$), which generate parasitic capillaries with spectrum (A8). Constant a in (A9) is the key tuning model constant. It must be chosen so as to get right value of the MSS; it is fixed at $a = 2\times10^{-3}$ [see *Yurovskaya et al*., 2013, for more details].

The filter function $\phi(k)$ restricts action of the parasitic capillaries source (A4). High-frequency cutoff of $\phi(k)$ must be linked to the transition wave number k_{bm} as $k_{pc}^h = k_\gamma^2/k_{bm}$, and its low-frequency cutoff is defined as $k_{pc}^l = (3/2)\,k_\gamma$ after comparison with the measurements [*Yurovskaya et al*., 2013]. Shape of the filter function is specified as:

$$\phi(k) = f\left[(k/k_{pc}^l)^2\right] - f\left[(k/k_{pc}^h)^2\right], \tag{A11}$$

with f defined by (A10).

Spectrum (A5) is valid in the equilibrium range of wind waves, i.e., far from the spectral peak. Full wave spectrum is a composition of the equilibrium spectrum $B_{sw}(\boldsymbol{k})$ and spectrum $B_{lw}(\boldsymbol{k})$ for energy containing waves proposed by *Donelan et al*. [1985]:

$$B(\boldsymbol{k}) = \chi B_{lw}(\boldsymbol{k}) + (1-\chi) B_{sw}(\boldsymbol{k}) \tag{A12}$$

where χ is a "cutoff" function suggested by *Elfouhaily et al*. [1997], which suppresses B_{lw} in the equilibrium range.

Acknowledgments
The core support of this study was provided by the Mega-Grant of the Russian Federation Government under grant 11.G34.31.0078, to support scientific research under the supervision of a leading scientist at Russian State Hydrometeorological University. This research was also supported by the European Space Agency (ESA) Support to Science Element (STSE) project OceanFlux-Greenhouse Gases (contract 4000104762/11/I-AM), and conducted in the context of the Ocean Flux GHG project supported by the European Space Agency through SOLAS STSE initiative. The support by the Russian Federal Program under contracts 14.B37.21.0619 and 14.B37.21.0673 are gratefully acknowledged.

References

Andreas, E. L. (2004), Spray stress revised, *J Phys. Oceanogr.*, *34*, 1429–1440.
Banner, M. L. (1990), The influence of wave breaking on the surface pressure distribution in wind wave interaction, *J. Fluid Mech.*, *211*, 463–495.
Banner, M. L., J. C. Trinder, and I. S. F. Jones (1989), Wave number spectra of short gravity waves, *J. Fluid Mech.*, *198*, 321–344, doi:10.1017/S0022112089000157.
Belcher, S. E., and J. C. R. Hunt (1993), Turbulent shear flow over slowly moving waves, *J. Fluid Mech.*, *251*, 109–148.
Chalikov, D., and V. Makin (1991), Models of the wave boundary layers, *Boundary Layer Meteorol.*, *56*, 83–99.
Chalikov, D., and S. Rainchik (2010), Coupled numerical modelling of wind and waves and the theory of the wave boundary layer, *Boundary Layer Meteorol.*, *138*, 1–41, doi:10.1007/s10546-010-9543-7.
Cox, C., and W. Munk (1954), Measurements of the roughness of the sea surface from photograms of the sun's glitter, *J. Opt. Soc. Am.*, *44*(11), 838–850.
Donelan, M. A. (1990), Air–sea interaction, in *The Sea, Ocean Engineering Science*, vol. 9, edited by B. LeMéhauté and D. Hanes, pp. 239–292, John Wiley, New York.
Donelan, M., J. Hamilton, and W. H. Hui (1985), Directional spectra of wind generated waves, *Philos. Trans. R. Soc. London, Ser. A*, *315*, 509–562.

Edson, J., V. Jampana, R. Weller, S. P. Bigorre, A. J. Plueddemann, C. W. Fairall, S. D. Miller, L. Mahrt, D. Vickers, and H. Hersbach (2013), On the exchange of momentum over the open ocean, *J. Phys. Oceanogr.*, *43*, 1589–1610, doi:10.1175/JPO-D-12-0173.1.

Elfouhaily, T., B. Chapron, K. Katsaros, and D. Vandermark (1997), A unified directional spectrum for long and short wind driven waves, *J. Geophys. Res.*, *102*(C7), 15,781–15,796.

Ericson, E. A., D. R. Lyzenga, and D. T. Walker (1999), Radar backscatter from stationary breaking waves, *J. Geophys. Res.*, *104*(C12), 29,679–29,695.

Fairall, C. W., E. F. Bradley, J. E. Hare, A. A. Grachev, and J. B. Edson (2003), Bulk parameterization of air–sea fluxes: Updates and verification for the COARE algorithm, *J. Clim.*, *16*, 571–591.

Fedorov, A. V., W. K. Melville, and A. Rozenberg (1998), An experimental and numerical study of parasitic capillary waves, *Phys. Fluids*, *10*, 1315.

Gemmrich, J. R., Banner M. L., and C. Garrett (1989), Spectrally resolved energy dissipation rate and momentum flux of breaking waves, *J. Phys. Oceanogr.*, *38*, 1296–1312.

Hara, T., and S. E. Belcher (2002), Wind forcing in the equilibrium range of wind-wave spectra, *J. Fluid Mech.*, *470*, 223–245.

Hara, T., and S. E. Belcher (2004), Wind profile and drag coefficient over mature ocean surface wave spectra, *J. Phys. Oceanogr.*, *34*, 2345–2358.

Hwang, P. A., B. Zhang, and W. Perrie (2010), Depolarized radar return for breaking wave measurement and hurricane wind retrieval, *Geophys. Res. Lett.*, *37*, L01604, doi:10.1029/2009GL041780.

Janssen, P. A. E. M. (1989), Wave-induced stress and the drag of air flow over sea waves, *J. Phys. Oceanogr.*, *19*, 745–754.

Kleiss, J. M., and W. K. Melville (2010), Observations of wave breaking kinematics in fetch-limited seas, *J. Phys. Oceanogr.*, *40*, 2575–2604, doi:10.1175/2010JPO4383.1.

Kudryavtsev, V. N. (2006), On effect of sea drops on atmospheric boundary layer, *J. Geophys. Res.*, *111*, C07020, doi:10.1029/2005JC002970.

Kudryavtsev, V., and J. Johannessen (2004), On effect of wavebreaking on short wind waves, *Geophys. Res. Lett.*, *30*, L20310, doi:10.1029/2409GL020919.

Kudryavtsev, V. N., and V. K. Makin (2001), The impact of the air flow separation on the drag of the sea surface, *Boundary Layer Meteorol.*, *98*, 155–171.

Kudryavtsev, V. N., and V. K. Makin (2004), Impact of swell on marine atmospheric boundary layer, *J. Phys. Oceanogr.*, *34*(4), 934–916.

Kudryavtsev V. N., and V. K. Makin (2011), Impact of ocean spray on the dynamics of the marine atmospheric boundary layer, *Boundary Layer Meteorol.*, *140*(3), 383–410, doi:10.1007/s10546-011-9624-2.

Kudryavtsev, V. N., V. K. Makin, and B. Chapron (1999), Coupled sea surface-atmosphere model. Part 2: Spectrum of short wind waves, *J. Geophys. Res.*, *104*(C4), 7625–7639.

Kudryavtsev, V., V. Dulov, V. Shrira, and V. Malinovsky (2008), On vertical structure of wind-driven sea surface currents, *J. Phys. Oceanogr.*, *38*(10), 2121–2144.

Kudryavtsev, V., A. Myasoedov, B. Chapron, J. Johannessen, and F. Collard (2012), Imaging meso-scale upper ocean dynamics using SAR and optical data, *J. Geophys. Res.*, *117*, C04029, doi:10.1029/2011JC007492.

Kudryavtsev, V., B. Chapron, A. Myasoedov, F. Collard, and J. Johannessen, (2013), On dual co-polarized SAR measurements of the Ocean surface, *IEEE Geosci. Remote Sens. Lett.*, *10*(4), 761–765, doi:10.1109/LGRS.2012.2222341.

Kukulka, T., and T. Hara (2008a), The effect of breaking waves on a coupled model of wind and ocean surface waves. Part I: Mature seas, *J. Phys. Oceanogr.*, *38*, 2145–2163, doi:10.1175/2008JPO3961.1.

Kukulka, T., and T. Hara (2008b), The effect of breaking waves on a coupled model of wind and ocean surface waves. Part II: Growing seas, *J. Phys. Oceanogr.*, *38*, 2164–2184, doi:10.1175/2008JPO3962.1.

Kukulka, T., T. Hara, and S. E. Belcher (2007), A model of the air–sea momentum flux and breaking-wave distribution for strongly forced wind waves, *J. Phys. Oceanogr.*, *37*, 1811–1828, doi:10.1175/JPO3084.1.

Longuet-Higgins, M. S. (1963), The generation of capillary waves by steep gravity waves, *J. Fluid Mech.*, *16*, 238.

Makin, V. K., and V. N. Kudryavtsev (1999), Coupled sea surface-atmosphere model. Part 1: Wind over waves coupling, *J. Geophys. Res.*, *104*(C4), 7613–7623.

Makin, V. K., and C. Mastenbroek (1996), Impact of waves on air-sea exchange of sensible heat and momentum, *Boundary Layer Meteorol.*, *79*, 279–300.

Makin, V. K., V. N. Kudryavtsev, and C. Mastenbroek (1995), Drag of the sea surface, *Boundary Layer Meteorol.*, *73*, 159–182.

Melville, W. K. (1977), Wind stress and roughness length over breaking waves, *J. Phys. Oceanogr.*, *7*, 702–710.

Munk, W. (2009), An inconvenient sea truth: Spread, steepness, and skewness of surface slopes, *Annu. Rev. Mar. Sci.*, *1*, 377–415, doi: 10.1146/annurev.marine.010908.163940.

Phillips, O. M. (1985), Spectral and statistical properties of the equilibrium range in the wind-generated gravity waves, *J. Fluid Mech.*, *156*, 505–531.

Plant, W. J. (1982), A relation between wind stress and wave slope, *J. Geophys. Res.*, *87*, 1961–1967.

Reul, N., H. Branger, and J.-P. Giovanangeli (2007), Air flow structure over short-gravity breaking water waves, *Boundary Layer Meteorol.*, *126*, 477–505, doi:10.1007/s10546-007-9240-3.

Romero, L., W. K. Melville, and J. M. Kleiss (2012), Spectral energy dissipation due to surface-wave breaking, *J. Phys. Oceanogr.*, *42*, 1421–1444.

Rozenberg, A., and M. Ritter (2005), Laboratory study of the fine structure of short surface waves due to breaking: Two-directional wave propagation, *J. Geophys. Res.*, *110*, C02011, doi:10.1029/2004JC002396.

Sullivan, P. P., J. C. McWilliams, and C.-H. Moeng (2000), Simulation of turbulent flow over idealized water waves, *J. Fluid Mech.*, *404*, 47–85.

Sutherland, P., and W. K. Melville (2013), Field measurements and scaling of ocean surface wave-breaking statistics, *Geophys. Res. Lett.*, *40*, 3074–3079, doi:10.1002/grl.50584.

Suzuki, N., T. Hara, and P. P. Sullivan (2013), Impact of breaking wave form drag on near surface turbulence and drag coefficient over young seas at high winds, *J. Phys. Oceanogr.*, *43*, 324–343, doi:10.1175/JPO-D-12-0127.1.

Vandemark, D., B. Chapron, J. Sun, G. H. Crescenti, and H. C. Graber (2004), Ocean wave slope observations using radar backscatter and laser altimeters, *J. Phys. Oceanogr.*, *34*, 2825–2842.

Veron, F., C. Hopkins, E. L. Harrison, and J. A. Mueller (2012), Sea spray spume droplet production in high wind speeds, *Geophys. Res. Lett.*, *39*, L16602, doi:10.1029/2012GL052603.

Walker, D. T., D. R. Lyzenga, E. A. Ericson, and D. E. Lund (1996), Radar backscatter and surface roughness measurements for stationary breaking waves, *Proc. R. Soc. London, Ser. A*, *452*, 1953–1984.

Yurovskaya, M. V., V. A. Dulov, B. Chapron, and V. N. Kudryavtsev (2013), Directional short wind wave spectra derived from the sea surface photography, *J. Geophys. Res.*, *118*, 4380–4394, doi:10.1002/jgrc.20296.